Modeling bismuth insertion in 1D hybrid lead halide pseudo-perovskite $TMSO(Pb_xBi_y)I_3$

Candida Pipitone[1], Federica Ursi[1], Francesco Giannici[1]*, Alessandro Longo[2], Antonietta Guagliardi[3], Norberto Masciocchi[4], Antonino Martorana[1]*

Abstract

The structure of the disordered 1D (pseudo-)perovskites $TMSO(Pb_xBi_y)I_3$ (TMSO = $(CH_3)_3SO^+$), obtained by doping the hybrid lead halide perovskite $TMSOPbI_3$ with Bi^{3+} ions, are investigated through the formulation of a statistical model of correlated disorder addressing the sequences of occupation of face-sharing BI_6 octahedra (B = Pb, Bi, or metal vacancy). The diffraction patterns simulated on the basis of the model are fitted to the experimental XRD traces, showing peaks with awkward (nearly trapezoidal) shape, under the assumption that the charge balance is fully accomplished within each chain. The analysis allowed to establish that only a fraction of the dopant can be allocated in the host matrix and that there is a definite tendency of the metal species to cluster as pure Pb and Bi sequences, the average lengths of which are calculated on the basis of the model.

Keywords: hybrid perovskites, face-sharing octahedra, lead halide; aliovalent doping, structural disorder, XRD whole pattern simulation

1. Introduction

Lead halide perovskites are steadily receiving increasing interest as semiconductor materials for applications in optoelectronics and energy harvesting [1-3]. Hybrid 3D perovskites of general formula ABX_3 are based on an inorganic backbone of corner-sharing BX_6^- octahedra hosting small A^+ organic cations in the cuboctahedral voids. The versatility of the structure enables the insertion of a wide variety of organic counterions by lowering, if necessary, the ideal cubic symmetry. As a consequence of hindrance, shape, or stoichiometric ratios of the precursors during synthesis, it is also possible to reduce the connectivity of the inorganic network down to 2D, 1D or 0D species [4-5]. The research on these low-dimensional frameworks is driven by the possibility of finely tuning the electronic structure, but also by their superior chemical, environmental and thermal stability with respect to 3D perovskites [6-9]. While recent studies about the structural and functional characterization of 2D (pseudo)perovskites are well documented, 1D analogues have received less attention. Inorganic threads constituted of corner-sharing octahedra belong to this latter class [10-12], but also edge- [13-14], and face-sharing backbones [15-18] are known.

A crucial issue about hybrid halide perovskites concerns the structural and functional modifications induced in these materials by doping, which can involve the A- and the B-sites, but also the halides shaping the octahedral cage. Tuning of electronic and optical properties obtained in this way is well documented for both 3D and lower-dimension halide perovskites: in some cases, the structural changes induced in the host matrix are negligible and can be ascribed to point defects, the interaction of which at increasing dopant concentration could be detrimental for the desired functional improvement [19]. Otherwise, depending on matrix connectivity and dopant concentration, it also happens that the structure of the pristine material is altered (as evidenced by noticeable changes of the X-ray diffraction patterns in 3D [20], 2D [21] and 1D [22] compounds) and the improvement of functional properties heavily depends on these structural

modifications. In these cases, the correlation of the atomic structure with the functional properties of the materials should be assessed, in particular with local techniques such as PDF (Pair Distribution Function) [20] or X-ray absorption spectroscopy [23]. However, to the best of our knowledge, this aspect has not been thoroughly investigated in the literature, even if it is highly relevant for the reliable assessment of structure-properties relationships. In this paper, we outline the structural analysis of bismuth insertion into $TMSOPbI_3$. The host compound is a 1D face-sharing pseudo-perovskite, the preparation, and characterization of which were recently reported based on a variety of experimental techniques and DFT modeling [22]. We present a structural model which accounts for the profound changes observed experimentally when lead is substituted at different concentrations by bismuth, giving rise to XRD peak shapes that are manifestly distorted by doping of the pristine host matrix. In particular, our analysis allows the determination of the average elemental composition of the crystals "seen" by diffraction and the depiction of the local structure of the doped compounds.

2. The model

The XRD patterns of $TMSOPbI_3$ at high Bi concentration show a striking modification of the diffraction profiles compared to the XRD patterns of the undoped samples (Figure 1). Some of these show a very peculiar peak shape deformation beyond the progressive changes of the lattice parameters at constant space group symmetry upon varying the Bi^{3+} concentration [22]. Such modifications are absent in the *0kl* reflections [22], which retain the sharp peak shape of the undoped material and do increase with the Miller index *h*. On increasing the bismuth content from the pristine all-Pb species, the peak shape of $h \neq 0$ reflections changes; as discussed below, this effect is attributed to the occurrence of non-random sequences of modified interatomic distances along the *a*-axis, when Pb^{2+} ions are substituted by Bi^{3+} and, concurrently, by charge-compensating vacant sites. Accordingly, our structural model is handled as a case of monodimensional correlated disorder and follows the formalism proposed more than 50 years ago by Kakinoki & Komura [24].

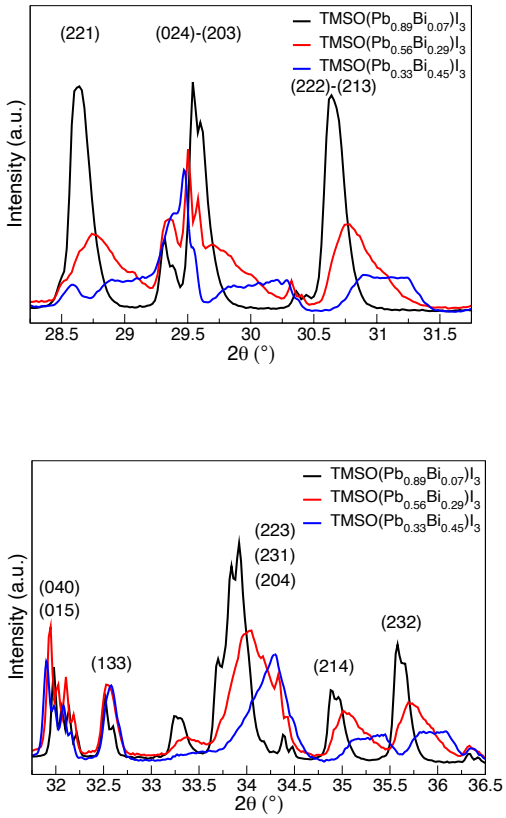

Figure 1. Experimental diffraction pattern in the angular ranges of interest for three different levels of Bi doping.

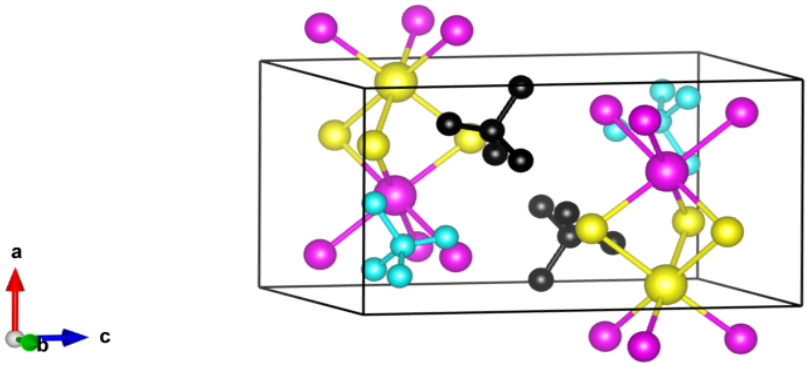

Figure 2. The two types of structural units of the model. Slice1: green-black; slice2: pink-blue. The alternate sequence along c of (green-black) and (pink-blue) generates the average structure. Note that the adjacent chain in the unit cell results from the inversion center (see text for details). Each BI3 pyramid may be populated by Pb, Bi or V. In the latter case, i.e., when the metal ion is missing, the chain of face-sharing octahedra is interrupted.

In our model, we describe the disordered structure of occupancy should comply with a range of statistical

$$\mathbf{P_0} = \begin{bmatrix} & PbPb & BiPb & VPb & BiBi & VBi & PbBi & PbV & BiV \\ PbPb & p^0_{11} & 0 & 0 & 0 & 0 & p^0_{16} & 1-p^0_{11}-p^0_{16} & 0 \\ BiPb & p^0_{21} & 0 & 0 & 0 & 0 & p^0_{26} & 1-p^0_{21}-p^0_{26} & 0 \\ VPb & p^0_{31} & 0 & 0 & 0 & 0 & p^0_{36} & 1-p^0_{31}-p^0_{36} & 0 \\ BiBi & 0 & p^0_{42} & 0 & p^0_{44} & 0 & 0 & 0 & 1-p^0_{16}-p^0_{44} \\ VBi & 0 & p^0_{52} & 0 & p^0_{54} & 0 & 0 & 0 & 1-p^0_{52}-p^0_{54} \\ PbBi & 0 & p^0_{62} & 0 & p^0_{64} & 0 & 0 & 0 & 1-p^0_{62}-p^0_{64} \\ PbV & 0 & 0 & p^0_{73} & 0 & 1-p^0_{73} & 0 & 0 & 0 \\ BiV & 0 & 0 & p^0_{83} & 0 & 1-p^0_{83} & 0 & 0 & 0 \end{bmatrix} \quad (1)$$

$TMSO(Pb_xBi_y)I_3$ (from now on 'T-$(Pb_xBi_y)I_3$')as being built by the alternate stacking along *a* of the "slices" drawn in Figure 1, each constituted by two TMSO molecules and two BI_3 "half-octahedra" (or pyramids), where B stands (in Kröger–Vink notation) for Pb^x_{Pb}, $Bi^{\bullet}_{Pb}$ or V''_{Pb}. Assuming that the charge balance is fully guaranteed within each chain of octahedra, the concentration of vacancies equals half the concentration of Bi^{3+} ions. The alternate stacking of the "slices" of Figure 2 is assumed to be a stochastic process. The thickness of each half octahedron is determined by the occupancy by Pb, Bi or V while, considering that the *0kl* lines keep a sharp profile independently of the Bi content, an average lateral hindrance is assumed. Hence, the model is referred to average *b*- and *c*- axis lengths and allows for local *a*-axis deviations from an average value. The trapezoidal shape of many peaks observed in the XRD patterns (see Figure 2) suggests the occurrence of a spread of different *a*-axis periodicities; accordingly, the sequences of Pb, Bi, or V influence reaching at least the second neighbor along *a*; otherwise, the XRD lines would be associated to a single average distance. The statistical events to be taken into consideration are then all the possible pairs of adjacent B site occupancies, each one characterized by its own "inter-cationic" distance (including vacant sites). Obviously, the VV couple cannot be considered, as it would generate an unphysical configuration of three isolated (unsupported) halides; on the other hand, the occurrence of a V''_{Pb} defect interrupts the chain. The transition probabilities between these events are then defined by the 8x8 stochastic matrix $\mathbf{P_0}$ (equation 1), where the headings of rows and columns represent the elementary events taking place along the $[BI_3]$ chain. According to the formalism of Kakinoki & Komura [24], the p^0_{ij} elements give the probability of concatenation between the *i*-th and the *j*-th couple: for instance, p^0_{16}

represents the probability of *PbPb-PbBi* concatenation, that is, the probability of a *Pb_Bi* sequence with *Pb* as antecedent second neighbour of *Bi*; p^0_{12} is null, as *PbPb* and *BiPb* do not concatenate, i.e., the last atom of *PbPb* does not coincide with the first atom of *BiPb*; $p^0_{16} \neq p^0_{26}$ as these probabilities, even if both relative to a first neighbour *Pb_Bi* transition, correspond to a different antecedent second neighbour of *Bi*, respectively, *Pb* and *Bi*.

As discussed above, the average structure is built by the alternate stacking of slice1 and slice2. This is allowed by defining the transition matrix **P**:

$$\mathbf{P} = \begin{bmatrix} \mathbf{0} & \mathbf{P^0} \\ \mathbf{P^0} & \mathbf{0} \end{bmatrix} \quad (2)$$

constituted by the blocks **0** and $\mathbf{P^0}$ of 8x8 matrices. The transition matrix **P** allows for 16 different events:

$1 \equiv Pb_2Pb_1$ $2 \equiv Bi_2Pb_1$ $3 \equiv V_2Pb_1$ $4 \equiv Bi_2Bi_1$ $5 \equiv V_2Bi_1$
$6 \equiv Pb_2Bi_1$ $7 \equiv Pb_2V_1$ $8 \equiv Bi_2V_1$ $9 \equiv Pb_1Pb_2$ $10 \equiv Bi_1Pb_2$
$11 \equiv V_1Pb_2$ $12 \equiv Bi_1Bi_2$ $13 \equiv V_1Bi_2$ $14 \equiv Pb_1Bi_2$ $15 \equiv Pb_1V_2$
$16 \equiv Bi_1V_2$

where the subscripts denote the classification as slice1 or slice2. **P** is still stochastic, its block structure allowing the alternate sequence of slice1 and slice2 that, like Lego bricks, produce the assembly of the octahedral BI_6 cages. As the sequence of octahedra occupancies is assumed to be a homogeneous Markov process, the elements of the n-th power of **P**, $\mathbf{P^n}$, define the transition probabilities after n successive stacking steps; the frequency of occurrence for each of the sixteen couples is obtained by solving the linear and homogeneous system of equations:

$$f_j = \sum_{i=1}^{16} f_i p_{ij} \quad (3)$$

where, due to the block structure (2),

$$f_i = f_{i+8}, \; i = 1,...8 \quad (4)$$

Moreover, the overall frequencies of Pb, Bi and V are easily calculated as:

$$\begin{aligned} f_{Pb} &= f_1 + f_2 + f_3 + f_9 + f_{10} + f_{11} \\ f_{Bi} &= f_4 + f_5 + f_6 + f_{12} + f_{13} + f_{14} \\ f_V &= f_7 + f_8 + f_{15} + f_{16} \end{aligned} \quad (5)$$

According to the K&K formalism [24], the intensity equation is given by:

$$I(\mathbf{q}) = Ntr(\mathbf{VF}) + \sum_{n=1}^{N-1}(N-n)tr(\mathbf{VFQ}^n) + c.c. \quad (6)$$

where **q** is the scattering vector, *N* is the number of stacked slices and the operator "*tr*" stands for matrix trace. The elements of V are defined as:

$$V_{ij} = V_i^* V_j \quad (7)$$

where the *V*'s are the scattering amplitudes of the slices, distinguished according to the octahedral site occupancies, and in particular:

$$\begin{aligned} &V_1, V_2, V_3, V_9, V_{10}, V_{11} \equiv V_{Pb} \\ &V_4, V_5, V_6, V_{12}, V_{13}, V_{14} \equiv V_{Bi} \\ &V_7, V_8, V_{15}, V_{16} \equiv V_V \end{aligned} \quad (8)$$

The **F** and **Q** matrix elements are defined by:

$$\left.\begin{aligned} F_{ij} &= f_i \delta_{ij} \\ Q_{ij} &= \sum_k \Phi_{ik} P_{kj} \\ \Phi_{ik} &= \exp(-i\phi_k \delta_{ik}) \end{aligned}\right\} \quad (9)$$

where $\phi_j = \mathbf{q}\cdot\mathbf{l}_j$ and $\mathbf{l}_j$ is the thickness of the *j*-th slice, depending on the octahedral site occupancy.

Going back to the general form of the $\mathbf{P^0}$ matrix (Equation (1)), some constraints on the parameter were introduced, on the basis of physical reliability (as results also from the computational analysis reported in [22-22a]), but also to limit correlations, to some extent unavoidable given the complexity of the model. In particular:

- BiBi_Bi is forbidden ($p^0_{44} = 0$, charge neutrality is assumede to be achieved locally);
- PbV_Pb and PbPb_V are forbidden ($p^0_{73} = 0$ involving also $p^0_{75} = 1$, $p^0_{17} = 0$ on the basis of computational evidences [22a]);
- VMe_V is forbidden ($p^0_{37} = p^0_{58} = 0$, the occurrence of isolated octahedra is discarded).

Overall, the number of independent probability parameters is reduced to 8, and the effective $\mathbf{P^0}$ matrix is:

$$\mathbf{P^0} = \begin{array}{c|cccccccc} & PbPb & BiPb & VPb & BiBi & VBi & PbBi & PbV & BiV \\ PbPb & p_{11} & 0 & 0 & 0 & 0 & p_{16} & 0 & 0 \\ BiPb & p_{21} & 0 & 0 & 0 & 0 & p_{26} & p_{27} & 0 \\ VPb & p_{31} & 0 & 0 & 0 & 0 & p_{36} & 0 & 0 \\ BiBi & 0 & p_{42} & 0 & 0 & 0 & 0 & 0 & p_{48} \\ VBi & 0 & p_{52} & 0 & p_{54} & 0 & 0 & 0 & 0 \\ PbBi & 0 & p_{62} & 0 & p_{64} & 0 & 0 & 0 & p_{68} \\ PbV & 0 & 0 & 0 & 0 & 1 & 0 & 0 & 0 \\ BiV & 0 & 0 & p_{83} & 0 & p_{85} & 0 & 0 & 0 \end{array}$$

The fitting of the model to the experimental data involves the simulation of the whole powder pattern and, therefore, also the definition of size, size distribution and shape of the diffracting domains, beside the evaluation of the spherical average of the intensity pattern defined in the three-dimensional reciprocal space. The latter task can be carried out by the Debye function analysis (DFA) [25-27]; however, in this case, due to the cumbersome statistical model and to the huge number of interatomic distances involved by the large crystallite size (≈100 nm), the conventional DFA approach is not computationally viable; therefore, we carried out the spherical average by numerical integration. Two further issues involved in the shaping of the model are: i. the symmetry of the octahedral coordination spheres, ii. the mutual shift along *a* of the two inorganic chains in the unit cell, and iii. the position of the TMSO molecules. Due to both the necessity of limiting the number of fitting parameters and to the advisability of excluding unphysical regions, the constraints imposed to the relative atomic positions by the Pnma symmetry of the undoped samples were maintained [22]; in particular, this choice implies that the two adjacent chains of BX_6 octahedra depicted in Figure 1 are related by an inversion center. While it seems quite reasonable that the same statistical rule governs both chains, it is also clear that the local structure, involving the deformation of the coordination polyhedra and the average orientation and mutual position of TMSO molecules, is only roughly represented by imposing an average symmetry relationship between the structural units of the investigated materials. The model provides satisfactory results (see below), though some residual discrepancies between the calculated patterns and the experimental data can be ascribed to the model approximations mentioned above.

3. Results and discussion

Figure 3 shows the results of the fitting procedure, carried out by χ^2 minimization in the angular range 26-37° 2θ, that is most relevant for the assessment of the parameters of the model. A whole 9-37° range is also shown in **Figure S1** for the T-$(Pb_{0.33}Bi_{0.45})I_3$ sample. It is evident that, even if not fully satisfactory, the model is able to reproduce the main features of the XRD data at different metal compositions giving rise to the quite different diffraction profiles shown in Figure 1. It is worth noticing that the constraint of the model to a first neighbour statistical influence (see Figure S1 as an example) gives clearly worse fittings. As concerns the shape of the octahedral cage, it was assumed that the lateral hindrance of the inorganic threads is fairly independent of the octahedra occupancy (see also Fig. 6 of [22], showing the substantial independency of the *b* and *c* axes on the metal composition). Then, the model is referred to average *b* and *c* lattice constants, while the actual height of the BI_3 pyramids is dependent on the contraction/expansion x_{Pb}, x_{Bi}, x_V parameters tuning the BI_3 vertical thickness as a function of the B occupancy. The average value <a> of the *a* axis is obtained by weighting the respective BI_3 thickness-related parameters a_{Pb}, a_{Bi} and a_V by the respective frequencies of occurrence of Pb, Bi and V in the doped compounds (Equation (5)). It is worth noticing that the values of a_{Pb}, a_{Bi} and a_V are in agreement with the idea that Bi^{3+} should involve an increased distance, with respect to Pb^{2+}, between

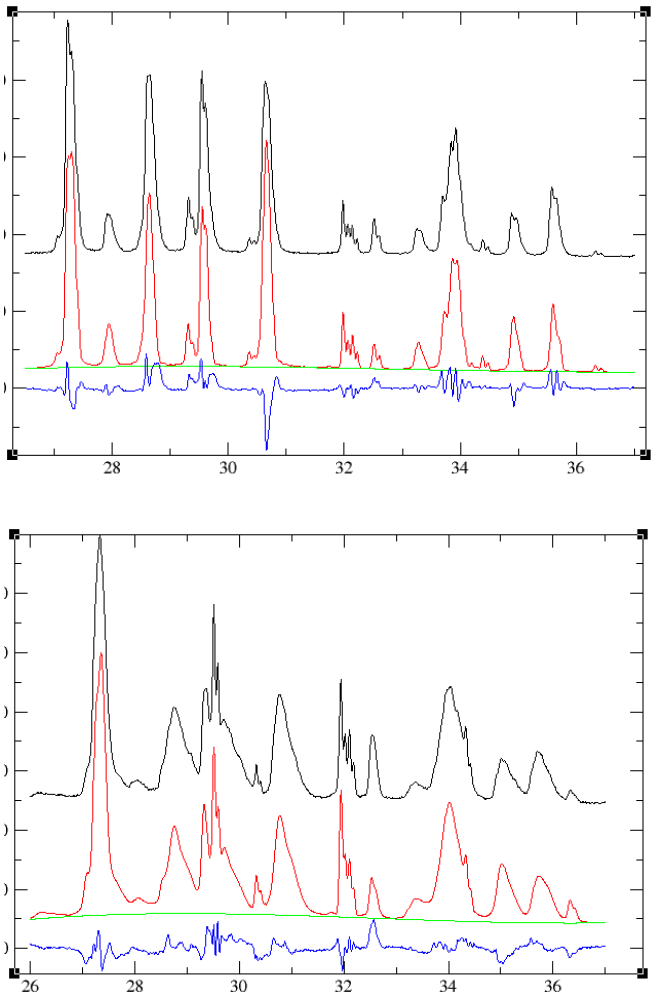

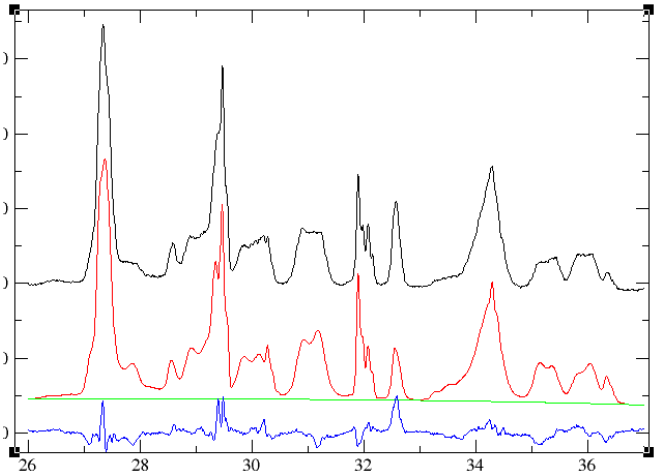

Figure 3. Experimental (black), fitted (red), background (green) and difference (blue) patterns for, from top to bottom, T-($Pb_{0.89}Bi_{0.07}$)I_3, T-($Pb_{0.56}Bi_{0.29}$)I_3 and T-($Pb_{0.33}Bi_{0.45}$)I_3.

Table 1. Values of the average refined lattice parameters (in Å) and of the local *a* axis values as a function of BI_3 occupancies.

	<*a*>*	*b*	*c*	a_{Pb}*	a_{Bi}*	a_V*
T-($Pb_{0.89}Bi_{0.07}$)I_3	7.7856(2)	11.198(2)	14.379(3)	7.7788(5)	7.9076(7)	7.5865(9)
T-($Pb_{0.56}Bi_{0.29}$)I_3	7.7057(3)	11.213(2)	14.396(2)	7.6108()	8.0305(2)	7.2653(2)
T-($Pb_{0.33}Bi_{0.45}$)I_3	7.6028(1)	11.212(1)	14.391(1)	7.5168(5)	7.8665(8)	7.5591(2)

* <*a*>: average *a*-axis length, obtained by weighting a_{Pb} , a_{Bi} , a_V (see text) with the respective frequencies of occurrence of Pb, Bi and V.

the centers of two face-sharing octahedra due to enhanced repulsion, while the presence of a vacancy produces a partial collapse of the octahedral cage. As a consequence of the local deformation of the octahedral cages, the effective *a* periodicity is ruled by the overall frequencies of occurrence of Pb, Bi and V (Equation (5)), in turn depending on the probability parameters defined in Equation (1). On the other hand, a rigid 'Lego model' should involve constant values of a_{Pb}, a_{Bi} and a_V irrespective of the sample compositions, and an average *a*-axis length depending only on the frequencies f_{Pb}, f_{Bi}, f_V. This is clearly not the case, as evidenced by the figures reported in Table 1, and also by a simulated pattern, reported in the Supporting Infos **Figure S2**, showing that a fitting carried out with constant 'Lego thicknesses' is far from the observed data. As a consequence, it is compulsory to conclude that <*a*> depends not only on the average composition but also on the local structure of the individual samples.

Table 2. Frequencies of occurrence of the elementary events defined in Equation (1) and of the overall frequencies f_{Pb}, f_{Bi}, f_V (Equation (5)).

	T-($Pb_{0.89}Bi_{0.07}$)I_3)	T-($Pb_{0.56}Bi_{0.29}$)I_3)	T-($Pb_{0.33}Bi_{0.45}$)I_3)
f_{PbPb}	0.8382	0.3378	0.4842
f_{BiPb}	0.0105	0.1275	0.1207
f_{VPb}	0.0000	0.0224	0.0490
f_{BiBi}	0.0437	0.1129	0.0576
f_{VBi}	0.0503	0.1451	0.0649
f_{PbBi}	0.0068	0.0868	0.1098
f_{PbV}	0.0040	0.0631	0.0599
f_{BiV}	0.0464	0.1044	0.0540
f_{Pb}	0.8487	0.4877	0.6539
f_{Bi}	0.1009	0.3449	0.2322
f_V	0.0504	0.1675	0.1139

By inspection of Table 2, it is worth to notice the fair agreement of the 2:1 ratios between bismuth and lead vacancies, confirming that the charge neutrality is

achieved within the inorganic threads. On the other hand, the relative Bi fractions, $f_{Bi}/(f_{Bi}+f_{Pb})$, are respectively 0.11, 0.41 and 0.26, far from the chemical analyses (from ICP data, respectively 0.08, 0.34 and 0.58 [22]), in particular for the latter. Taking into account that the fitted patterns reported in Figure 3 seem to reproduce the peculiar behaviour of the experimental data, and that forcing the metal fractions to the chemical analysis values yields definitely worse fittings (see, as an example, **Figure S3**), it should be concluded that the XRD patterns are sensitive to only a fraction of the whole sample, likely the one corresponding to the larger crystallites. As concerns the opposite behaviour of the T-$(Pb_{0.56}Bi_{0.29})I_3$ and T-$(Pb_{0.33}Bi_{0.45})I_3$ samples, the main difference is relative to the definitely higher frequencies of the couples BiBi, BiV and VBi, which could be indicative of a BiBi preferential clusterization neutralized by a neighbouring Pb vacancy. This clusterization could be effective in stabilizing the insertion of Bi into the TMSO-(lead iodide) framework and provide an interpretation relative to the occurrence of a definitely larger a_{Bi} value for the T-$(Pb_{0.56}Bi_{0.29})I_3$ sample (Table 1).

In summary, the structural model described in this paper was applied to the analysis of monodimensional correlated disorder in 1D hybrid halide aliovalent doped (pseudo)perovskites; the good fittings reported in the body of the paper, but also the bad ones reported in the supporting infos demonstrate that different local structures are compatible with macroscopic parameters such as the overall chemical composition or the average axes lengths and then, in establishing structure-properties correlations a detailed analysis of the fine structural details are necessary.

We point out that monodimensional disorder could be relevant in doped layered halide perovskites as well, and that the approach outlined in this paper could be easily extended to these cases. There is an extensive literature investigating the effects of doping on stability and functional properties of hybrid halide perovskites with several experimental and computational techniques (see, for recent accounts, the reviews by Krishnamurthy et al. and Su et al.30,31), but studies concerning the assessment of well-established relationships with the atomic structure are lacking. The relevance of this topic begins to be acknowledged in recent papers 20-23; thus, this paper is a further contribution in this direction.

References

[1] Kim J Y, Lee J, Jung H S, Shin H and Park N 2020 High-Efficiency Perovskite Solar Cells. *Chem. Rev.* **120**, 7867.

[2] Ke W and Kanatzidis M G 2019 Prospects for low-toxicity lead-free perovskite solar cells *Nat. Commun.* **10** 965.

[3] Xiong Y, Xu L, Wu P, Sun L, Xie G and Hu B 2019 Bismuth Doping–Induced Stable Seebeck Effect Based on MAPbI3 Polycrystalline Thin Films *Adv. Funct. Mater.* **29** 900615.

[4] Mao L, Tsai H, Nie W, Ma L, Im J, Stoumpos C C, Malliakas C D, Hao F, Wasielewski M R, Mohite A D and Kanatzidis M G 2016 Role of Organic Counterion in Lead- and Tin-Based Two-Dimensional Semiconducting Iodide Perovskites and Application in Planar Solar Cells. *Chem. Mater.* **28**, 7781.

[5] Fateev S A, Petrov A A, Marchenko E I, Zubavichus Y V, Khrustalev V N, Petrov A V, Aksenov S M, Goodilin E A and Tarasov A B 2021 FA_2PbBr_4: Synthesis, Structure, and Unusual Optical Properties of Two Polymorphs of Formamidinium-Based Layered (110) Hybrid Perovskite. *Chem. Mater*. **33**, 1900.

[6] Zhou Y, Chen J, Bakr O M and Sun H-T 2018 Metal-Doped Lead Halide Perovskites: Synthesis, Properties, and Optoelectronic Applications. *Chem. Mater*. **30**, 6589.

[7] Jiang J, Liu F, Tranca I, Shen Q and Tao S 2020 Atomistic and Electronic Origin of Phase Instability of Metal Halide Perovskites *ACS Appl. Energy Mater.* **3** 11548.

[8] (8) Parashar M, Singh R, Yoo K and Lee J-J 2021 Formation of 1-D/3-D Fused Perovskite for Efficient and Moisture Stable Solar Cells. *ACS Appl. Energy Mater*. **4**, 2751.

[9] Elsenety M M, Antoniadou M, Balis N, Kaltzoglou A, Sygellou L, Stergiou A, Tagmatarchis N and Falaras P 2020 Stability Improvement and Performance Reproducibility Enhancement of Perovskite Solar Cells Following $(FA/MA/Cs)PbI_3{-}xBr_x/(CH_3)_3SPbI_3$ Dimensionality Engineering *ACS Appl. Energy Mater*. **3**, 2465

[10] Tao K, Li Y, Ji C, Liu X, Wu Z, Han S, Sun Z and Luo J 2019 A Lead-Free Hybrid Iodide with Quantitative Response to X-ray Radiation *Chem. Mater*. **31**, 5927.

[11] Fabian D M, Ganose A M, Ziller J W, Scanlon D O, Beard M C and Ardo S 2019 Influence of One Specific Carbon–Carbon Bond on the Quality, Stability, and Photovoltaic Performance of Hybrid Organic–Inorganic Bismuth Iodide Materials *ACS Appl. Energy Mater.* **2** 1579.

[12] Yu S-K, Xu N-N, Jiang M, Weng Y-G, Zhu Q-Y and Dai J 2020 Hybrid Lead Iodide Perovskites with Mixed Cations of Thiourea and Methylamine, From One Dimension to Three Dimensions. *Inorg. Chem*. **59** 15842.

[13] Yuan H, Massuyeau F, Gautier N, Kama A B, Faulques E, Chen F, Shen Q, Zhang L, Paris M and Gautier R 2020 Doped Lead Halide White Phosphors for Very High Efficiency and Ultra-High Color Rendering *Angew. Chem. Int. Ed.* **59** 2802.

[14] Kaltzoglou A, Stoumpos C C, Kontos A G, Manolis G K, Papadopoulos K, Papadokostaki K G, Psycharis V, Tang C C, Jung Y-K, Walsh A, Kanatzidis M G and Falaras P 2017 Trimethylsulfonium Lead Triiodide: An Air-Stable Hybrid Halide Perovskite. *Inorg. Chem*. **56**, 6302.

[15] Zhang W-F, Pan W-J, Xu T, Song R-Y, Zhao Y-Y, Yue C-Y and Lei X-W 2020 One-Dimensional Face-Shared Perovskites with Broad-Band Bluish White-Light Emissions. *Inorg. Chem*. **59** 14085.

[16] Wilke M and Casati N 2018 Insight into the Mechanochemical Synthesis and Structural Evolution of Hybrid Organic–Inorganic Guanidinium Lead(II) Iodides. *Chem. Eur. J*. **24** 17701.

[17] Pipitone C, Giannici F, Martorana A, Bertolotti F, Calabrese G, Milita S, Guagliardi A, Masciocchi N 2021 Proton Sponge Lead Halides containing 1D Polyoctahedral chains *CrystEngComm* **23**, 1126.

[18] Khan M E, Lee J, Byeon S and Kim Y-H 2019 Semimetallicity and Negative Differential Resistance from Hybrid Halide Perovskite Nanowires *Adv. Funct. Mater*. **29** 1807620.

[19] Liu Y, Wang C, Zhou C, Li P, Zhu L, Sun S, Feng X, Sun Y and Zhao G 2020 Mechanism for tunable broadband white photoluminescence of one-dimensional $(C_4N_2H_{14})_2Pb_{1-x}Mn_xBr_4$ perovskite microcrystals *J. Lumin.* **221** 117045.

[20] Spanopoulos I, Hadar I, Ke W, Guo P, Mozur E M, Morgan E, Wang S, Zheng D, Padgaonkar S, Manjunatha Reddy G N, Weiss E A, Hersam M C, Seshadri R, Schaller R D and Kanatzidis M G 2021 Tunable Broad Light Emission from 3D "Hollow" Bromide Perovskites through Defect Engineering *J. Am. Chem. Soc.* **143**, 7069.

[21] Cortecchia D, Mròz W, Neutzner S, Borzda T, Folpini G, Brescia R and Petrozza A 2019 Defect Engineering in 2D Perovskite by Mn(II) Doping for Light-Emitting Applications *Chem* **5** 2146.

[22] Pipitone C, Giannici F, Martorana A, García-Espejo G, Carlotto S, Casarin M, Guagliardi A and Masciocchi N 2021 Heterovalent BiIII/PbII ionic substitution in one-dimensional trimethylsulfoxonium halide pseudo-perovskites (X = I, Br). *J. Phys. Chem. C* **125**, 11728.

[23] Serrano-Sanchez F, Conesa J C, Rodrigues J E, Marini C, Martínez J L and Alonso J A 2020 Divalent chromium in the octahedral positions of the novel hybrid perovskites $CH_3NH_3Pb_{1-x}Cr_x(Br,Cl)_3$ (x=0.25, 0.5): Induction of narrow bands inside the bandgap J. *Alloys Compd*. **821**, 153414.

[24] Kakinoki J and Komura Y 1965 Diffraction by a One-Dimensionally Disordered Crystal. I. The Intensity Equation. *Acta Cryst*. **19** 137.

[25] Longo A, Sciortino L, Giannici F and Martorana A 2014 Crossing the boundary between face-centred cubic and hexagonal close packed: the structure of nanosized cobalt is unraveled by a model accounting for shape, size distribution and stacking faults, allowing simulation of XRD, XANES and EXAFS *J. Appl. Cryst*. **47**, 1562.

[26] Longo A, Giannici F, Sciortino L and Martorana A 2020 A real-space approach to the analysis of stacking faults in close-packed metals: G(r) modelling and Q-space feedback *Acta Cryst.* **A76** 84.

[27] Bertolotti F, Moscheni D, Migliori A, Zacchini S, Cervellino A, Guagliardi A and Masciocchi N 2016 A total scattering Debye function analysis study of faulted Pt nanocrystals embedded in a porous matrix *Acta Cryst*. **A72**, 632.

[28] Bartolomé J, Climent-Pascual E, Redondo-Obispo C, Zaldo C, Alvarez A L, de Andrés A and Coya C 2019 Huge Photostability Enhancement in Bismuth-Doped Methylammonium Lead Iodide Hybrid Perovskites by Light-Induced Transformation *Chem. Mater*. **31**, 3662.

[29] Xiong Y, Xu L, Wu P, Sun L, Xie G and Hu B 2019 Bismuth Doping–Induced Stable Seebeck Effect Based on MAPbI3 Polycrystalline Thin Films *Adv. Funct. Mater*. **29**, 1900615.

[30] Krishnamurthy S, Pandey P, Kaur J, Chakraborty S, Nayak P K, Sadhanala A and Ogale S 2021 Organic–inorganic hybrid and inorganic halide perovskites: structural and chemical engineering, interfaces and optoelectronic properties *J. Phys. D: Appl. Phys.* **54**, 133002.

[31] Su B, Zhou G, Huang J, Song E, Nag A and Xia Z 2021 Mn^{2+}-Doped Metal Halide Perovskites: Structure, Photoluminescence, and Application *Laser Photon. Rev*. **15** 2000334.

Supporting infos.

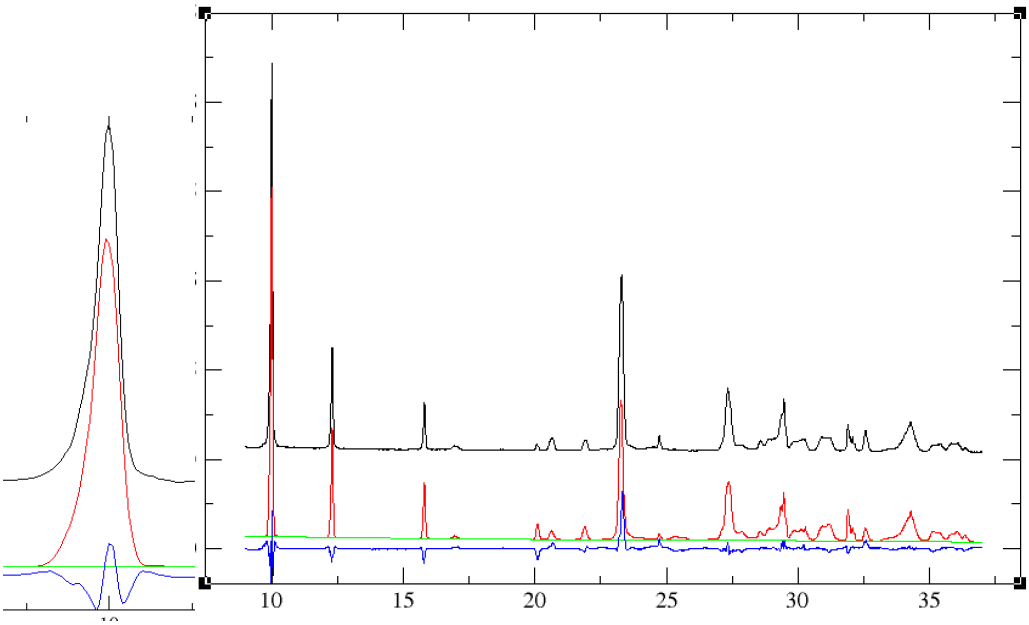

Figure S1. Fitting to the experimental pattern of sample T-($Pb_{0.56}Bi_{0.29}$)I_3 in the 2theta interval 9-37°. The inset shows the detail relative to the (011) line at about 10° 2θ, where the simulation of horizontal and vertical incident beam divergences are strongly effective.

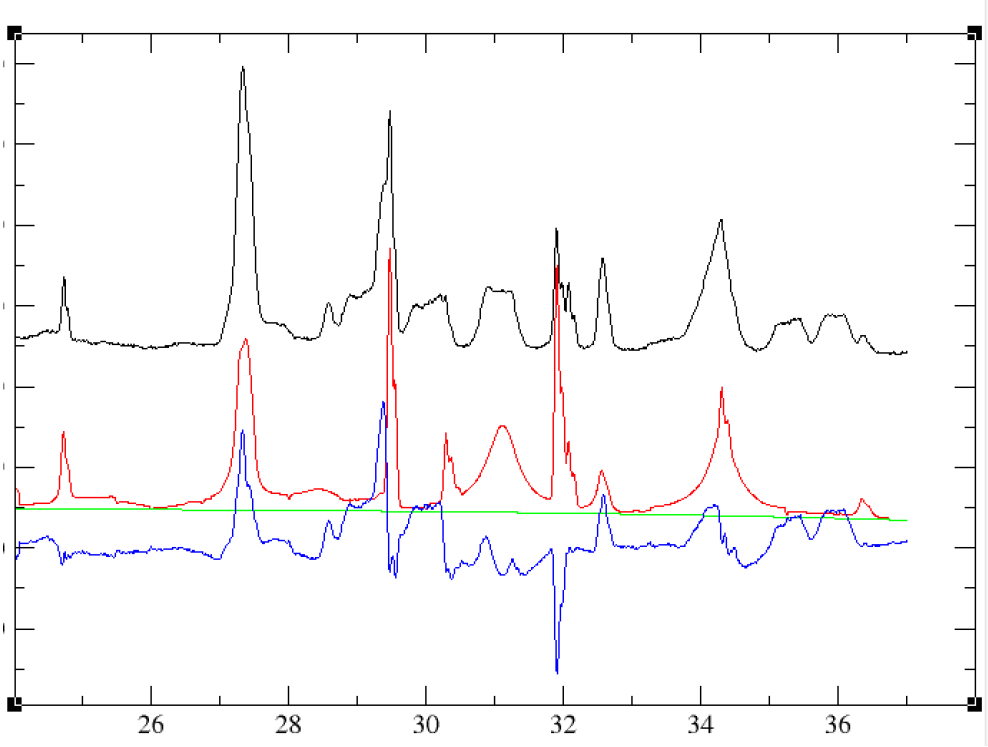

Figure S2. Fitting to the XRD pattern of sample T-($Pb_{0.56}Bi_{0.29}$)I_3. The calculated pattern was obtained with blocked a_{Pb}, a_{Bi} and a_V . These values were determined as the best ones giving simultaneosly the observed a-axis average lengths for all the three investigated samples.

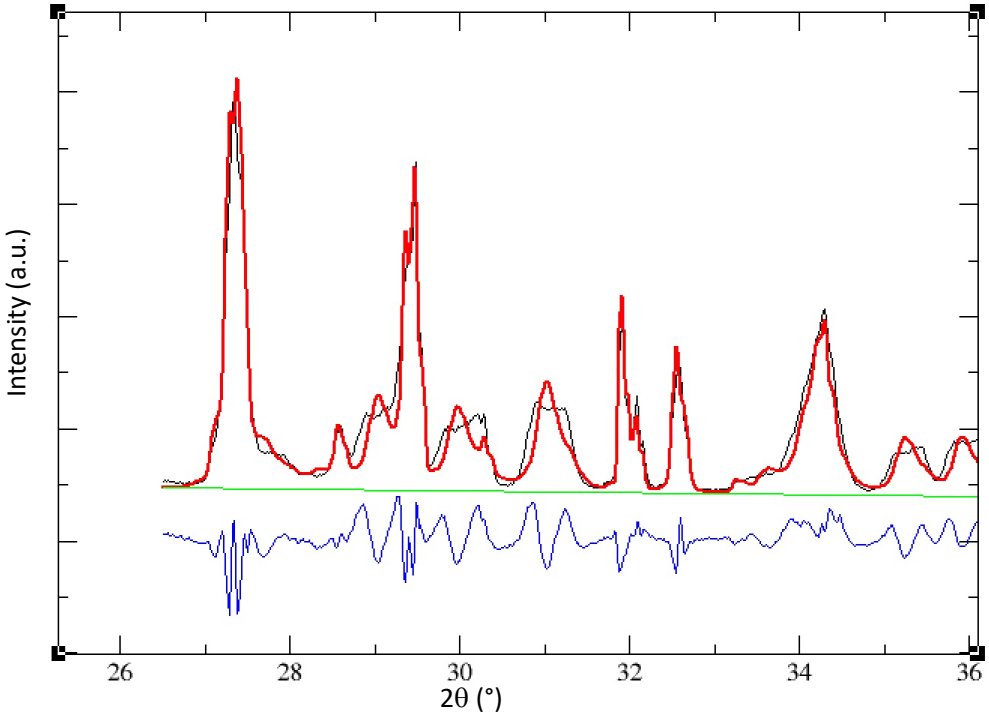

Figure S3. Fitting run relative to the sample T-(Pb0.33Bi0.45)I3, constraining the model to the analytical composition.